Towards a superconducting microbridge single photon detector

Koh Ming Zhi, Darren

A0181322R

Department of Physics, Faculty of Science

National University of Singapore

Supervisor:

Prof. Christian Kurtsiefer

In partial fulfillment of the requirements for the degree of

Bachelor of Science (Hons)

2022

Acknowledgments

First, I would like to thank Lijiong for guiding me throughout this entire process. Even though I might ask many basic and repetitive questions, you patiently explained them to me. Without you, I would have never become the experimentalist I am today.

Next, I would like to thank Prof Christian Kurtsiefer for accepting me into his lab. Without you, this opportunity would have never been possible.

To all other QO lab members, especially the other FYP students, thank you for making my experience so much more enjoyable and memorable.

"For this journey's end is but one step forward to tomorrow"

Abstract

As of today, high detection efficiency of single photons at the telecom wavelengths can only be done using superconducting nanowire detectors. However, their design requiring the use of long and thin meandering wires to increase their active area limits their maximum count rate. Research in recent years suggests a new geometry, the microbridge, that would allow for a wider and shorter superconducting detector with a larger maximum count rate. In this thesis, we present our work on the characterization of superconducting microbridge detectors and the construction of a spontaneous parametric down conversion pair source that can be used for characterization of single photon detectors. The detectors was characterized to have a detection efficiency of $10^{-4}\,\%$ and a timing jitter of $\approx 141\,\mathrm{ps}$. The source was characterized to have a pair rate of $4 \times 10^{5}\,\mathrm{pairs\,s^{-1}\,mW^{-1}}$.

Contents

Chapter 1

Introduction

The concept of the photon, the quantization of light, was first introduced by Max Planck and Albert Einstein in the early 20th century as an explanation for black-body radiation and the photoelectric effect respectively. However, it was not until the 1930s with the invention of the photomultiplier tube that single photon detection was realized. Since then, single photon detection technology has matured greatly, with the invention of the single photon avalanche diode and superconducting nanowire detectors. In the years after the nanowire, further research in modeling its detection mechanism have led to the development of a new geometry for superconducting detectors, the microbridge, which was demonstrated in 2018. But before introducing this, I will first give a brief qualitative overview of current detector technologies and compare them using their figures of merit.

1.1 Detector technologies

Photomultiplier tube

A photomultiplier tube (PMT) works by using the photoelectric effect to produce and then amplify photoelectrons into a measurable current pulse.

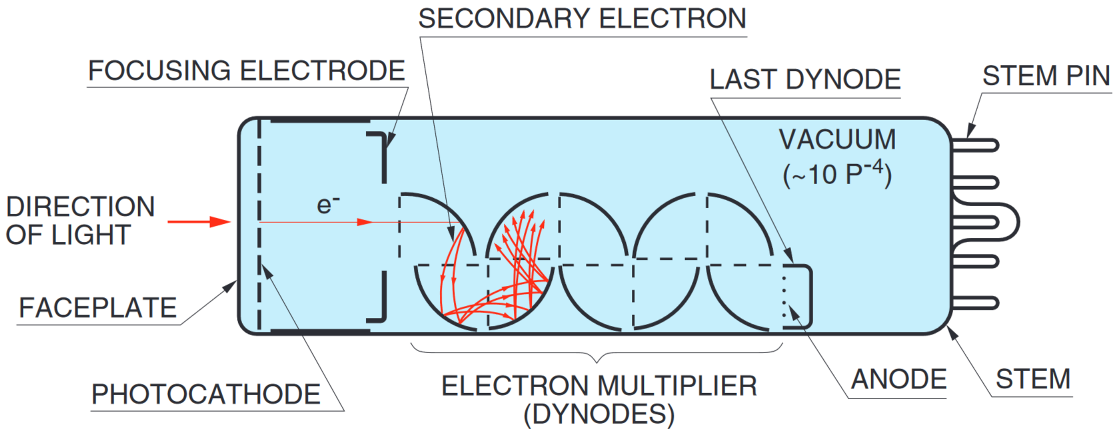

Figure 1.1: Schematic of a photomultiplier tube. Figure taken from [20]

Photons that enters the PMT falls on the photocathode, producing electrons through the photoelectric effect. Then, as the dynodes are at a higher potential relative to the cathode, the electrons accelerate towards the dynodes. Upon hitting the dynode, it will emit several electrons, amplifying the initial electron count. This process repeats for the subsequent dynodes which are at a higher potential relative to the earlier dynode, resulting in a current amplification of 10 to 10^8 times. These electrons are then collected at the cathode which is measured as a sharp current pulse.

Single photon avalanche diode

The simplest model of a single photon avalanche diode (SPAD) would consist of a p-n junction diode in reverse bias. A photon falling on the depletion region of the diode excites an electron, producing an electron hole pair. Due to the large electric field in this region, the electron accelerates towards the n-type region and along the way, it might collide with others atoms in the depletion region. If sufficient energy is imparted from this collision, more electron hole pairs may be produced. This process will then repeat resulting in an electron avalanche that is measurable as a current pulse.

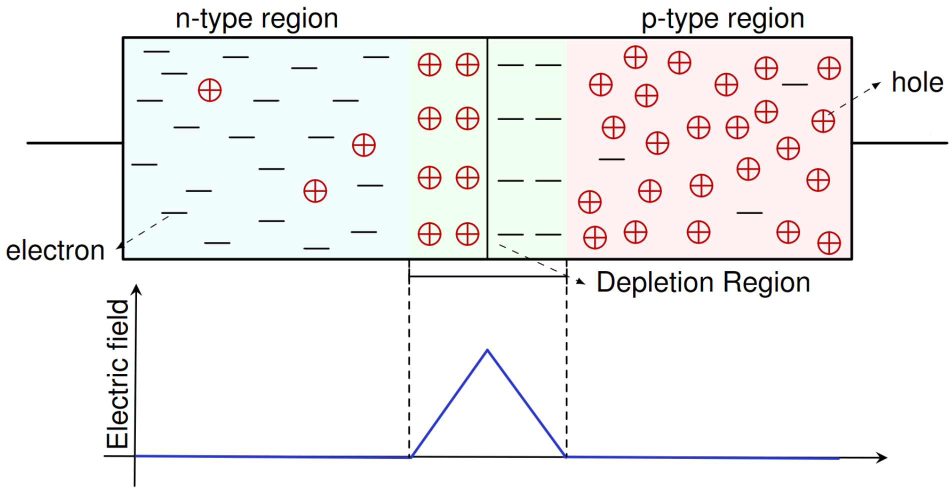

Figure 1.2: Schematic of a p-n junction with the corresponding electric field profile. Figure taken from [15]

Superconducting detectors

The superconducting nanowire single photon detector (SNSPD) is a long meandering superconducting strip with a typical width on the order of 100 nm. It is biased with a current just below its critical current, the maximum current it can carry before losing superconductivity. When a sufficiently energetic photon is absorbed by the detector, the cooper pairs gets excited and depairs into quasiparticles. This results in a loss of superconductivity in a small region, typically called a hotspot, forcing most of the current to flow around it. The current density in the surrounding increases beyond the critical current density, causing it to turn non-superconducting and form a non-superconducting band. The increase in resistance reduces the amount of current that can flow across it and forces some current to get reflected back. This reflected current pulse is then read out as the detector response.

The model described was first used in the seminal paper that demonstrated the use of superconducting nanowires as single photon detectors and is accurate enough for most explanations [14, 29]. However, it places a limitation on the size of the nanowire, requiring it to be around the same size of the hotspot for the band to form. As such, a long meandering design is required to achieve a large active area. Since then, further research and analysis using non-equilibrium superconductivity has led to another explanation for the detection mechanism. This new model allows for a different detector geometry with a larger width and could be used to explain the working principles of microbridge detectors in this project.

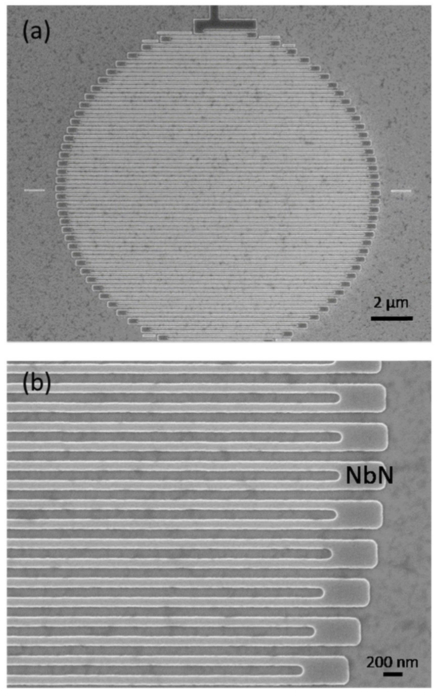

Figure 1.3: Scanning electron microscope image of a superconducting nanowire detector. Figure taken from [23].

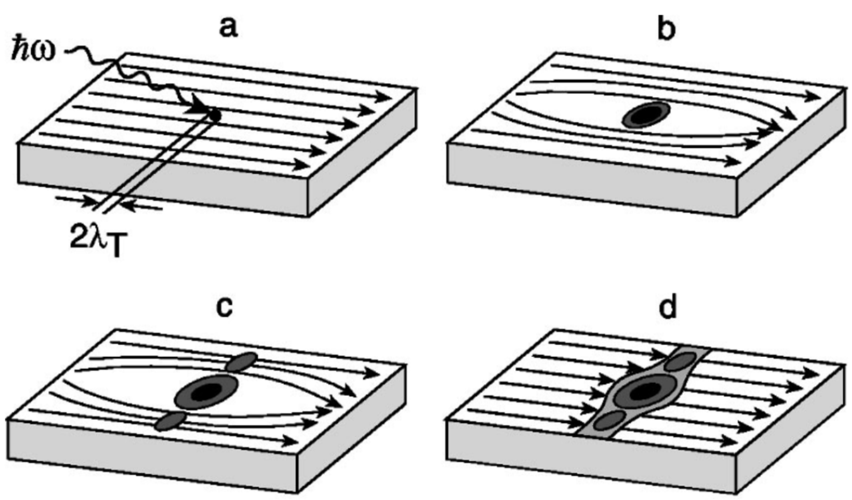

Figure 1.4: Formation of a non-superconducting band across a superconducting nanowire. Figure taken from [14].

1.2 Detector figures of merit

Some commonly used figures of merit in comparing detectors are

- Detection efficiency: The probability of detecting a photon. This can be split into the detector intrinsic efficiency, the probability of the detector absorbing the photon and producing a response, and the coupling efficiency, the percentage of light that falls on the detector active area from the detector waveguide.
- Maximum count rate: The maximum number of photons the detector can detect in a second.
- Dark counts: The number of false counts produced by the detector when no light is present.
- Timing jitter: The variation in the timing delay between the arrival of the photon and the detector response. This is typically quantified using the full width half maximum (FWHM) of this distribution.

Among these, dark counts and timing jitter are two essential parameters that may not attract enough attention for many users.

Dark counts are undesirable as they may make it difficult to distinguish true photon counts. For example, if we were measuring a weak light source that produces only $50\,\mathrm{photons\,s^{-1}}$ with a detector that has a dark count rate of $10^3\,\mathrm{counts\,s^{-1}}$. The statistical fluctuations of the dark counts would dominate over the counts due to the photons.

Minimizing timing jitter is important in applications such as time-resolved fluorescence spectroscopy and clock synchronization [17, 27]. In fluorescence spectroscopy, fluorophores are excited repeatedly with a pulsed laser and a single photon detector is used to detect the fluorescence. The timing difference between the pulse production and the fluorescence detection is used to calculate the fluorescence lifetime and the decay profile. In clock synchronization, a tightly time correlated photon pair is split and sent to two parties who detect them with single photon detectors. Then, clock synchronization is done by comparing the photon detection times. In both use cases, jitter introduces uncertainty to the detection timing and limits the precision achievable.

1.3 Comparison between detectors

One of the main reasons to research and develop superconducting detectors are the low detection efficiency of PMTs and SPADs in the infrared region. This is especially important given that telecommunication over fiber uses light in the 1260 nm to 1675 nm region. As of today, PMTs using a mixture of indium phosphide (InP) and indium gallium arsenide (InGaAs) as the photocathode can only achieve an efficiency of around 2 % [19]. InGaAs SPADs while better, only have efficiencies around 10 % to 20 % [8]. On the other hand, SNSPDs have demonstrated efficiencies of more than 90 % at telecom wavelengths [36]. Superconducting microbridges have also demonstrated efficiencies over 90 % [35].

However, one problem faced by SNSPDs is its dead time on the order of 10 ns, which limits its maximum count rate to around $10^7\,\mathrm{s}^{-1}$. The microbridge on the other hand have much a much shorter dead time of on the order of 100 ps giving it a maximum count rate that is two orders of magnitude more than SNSPDs. Furthermore, the larger size of microbridges could also allow it to potentially be manufactured by the cheaper and faster photolithography technique compared to the electron-beam lithography required for the nanowire.

1.4 Outline of thesis

In this thesis, we will describe the development of the setup used to characterize our superconducting microbridge detector. In chapter 2, we introduce the operating principles of superconducting detectors in more detail. In chapter 3, we will go over the methods used to couple light from optical fibers onto the detector. In chapters 4 and 5, we cover the construction of a polarization entangled photon pair source that can be used to characterize our detector. Next, chapter 6 will cover the measurement results of the detector. Finally, we conclude in chapter 7 and end with some remarks and outlook.

Chapter 2

Superconducting microbridge detectors

In this chapter, we will work towards understanding the operating principles of superconducting detectors. But before that, we need to introduce some basic superconductivity theory.

2.1 Superconductivity

A material is superconducting if when cooled below a certain temperature it displays the following two properties. Its electrical resistance vanishes and it exhibits the Meissner effect, the expulsion of the magnetic field from the material. This temperature is its critical temperature. The theory behind superconductivity is interesting but is unfortunately beyond the scope of this thesis, however interested readers may pursue this topic in [28, 34]. Even so, some basic terms and ideas is required to understand how superconducting detector works. As most of the literature on the detectors make use of the phenomenological Ginzburg-Landau (GL) theory of superconductivity, we will focus on that in this chapter.

GL theory assumes that the current in superconductors is described similarly to current in metals, where charge carriers are free electrons with charge e, mass m_{e} and density n_{e}. For superconductors, we have charge carriers with charge, e^*, mass m^* and density, n_{s}^*. This density is described using a complex valued order parameter, ψ, which is defined as,

$$|\psi|^2 = n_{\mathrm{s}}^* \ . \tag{2.1}$$

Experimentally it was found that $e^* = 2e$, $m^* = 2m_{\mathrm{e}}$, $n_{\mathrm{s}}^* = \frac{1}{2}n_{\mathrm{s}}$. Meaning that the carriers are not free electrons but rather electrons pairs which are the cooper pairs derived from the Bardeen-Cooper-Schrieffer (BCS) theory.

2.2 Microbridge properties

Before discussing the detection mechanism, it will be useful to introduce the structure of the microbridge and detector circuit to provide some context. The detector is made by our collaborators at the Centre for Disruptive Photonic Technologies at Nanyang Technological University. It consists of a thin 6 nm niobium titanium nitride (NbTiN) film on a silicon (Si) substrate with a distributed bragg reflector coating in between. The NbTiN film is patterned into a constriction-type bridge using electron beam lithography. This topology was chosen to prevent current crowding which reduces the critical current in the detector [6]. At its thinnest, the bridge has a width of 2 µm which translates to an active area of around 2 µm × 2 µm. The detector is housed within the 4 K cooling stage of a cryogenic fridge with a typical temperature of around 3.3 K.

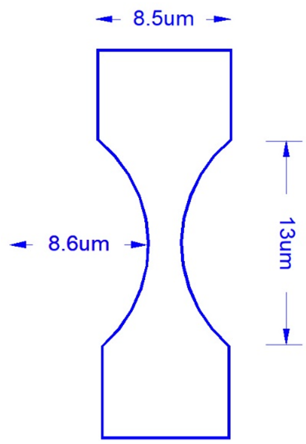

Figure 2.1: Constriction-type topology of microbridge detector.

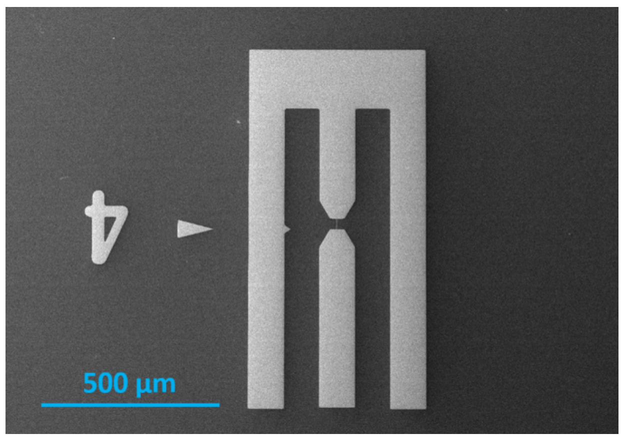

Figure 2.2: Scanning electron microscope image of microbridge (medium grey) together with electrical contacts (light grey) on Si wafer (dark grey). Outer contacts are connected to ground and middle contact is used to bias the detector.

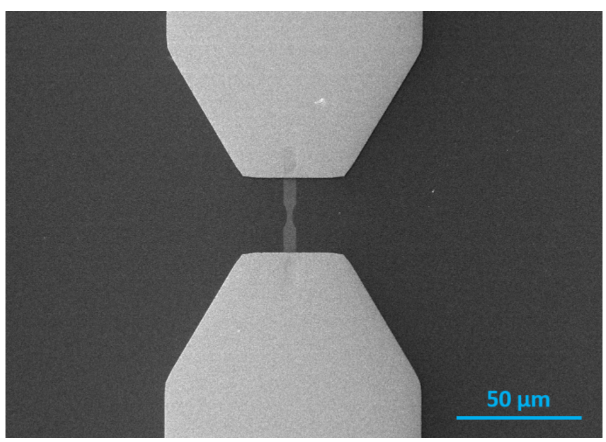

Figure 2.3: Closeup image showing the size of the detector relative to the electrical contacts.

2.3 Detector circuitry

The circuit used can be broken down into three parts connected using a bias tee. A bias tee is a three port device which can be used to combine or split the direct current (DC) and alternating current (AC) components of a signal. These ports are commonly referred to as the DC port, radio frequency (RF) port and the DC + RF port. The DC port only allows the DC component through, the RF port only allows the AC component through and the combined port allows both DC and AC components through. This behavior allows it to be modeled like in the diagram with an inductor on the DC port and capacitor on the RF port.

First, connected to the DC port is the constant current source for biasing the detector. This is done using a constant voltage source with a resistor in series. Next, connected to the RF port is the amplifier which is used to amplify the current pulse from the detector. Lastly, the detector itself with a shunt resistor in parallel is connected to the DC+RF port by a transmission line. This same circuit can be used for a nanowire detector, just with the removal of the shunt resistor.

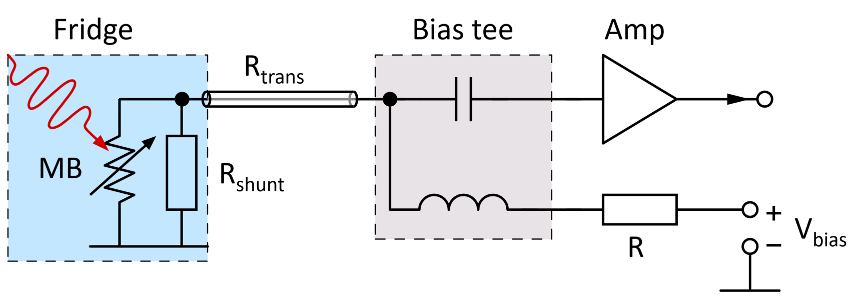

Figure 2.4: Circuit used to bias and readout detector response. The microbridge (MB) and shunt resistor are located in the fridge while the rest are at room temperature.

2.4 Detection mechanism

The detection mechanism of a superconducting nanowire or microbridge can be broken up into three parts. The formation of a hotspot upon absorption of a photon, the growth of a non-superconducting band, and the resetting of the detector back into its superconducting state.

First, the absorption of a photon excites cooper pairs in the superconductor, causing it to depair into quasiparticles. These quasiparticles then collide into other cooper pairs causing them to depair producing more quasiparticles. This produces a region with suppressed order parameter called a hotspot. The growth of this hotspot can be described macroscopically by the heat flow equation,

$$Cd\frac{\partial T}{\partial t} = \kappa d\nabla^2 T + \alpha(T - T_0) \ , \tag{2.2}$$

where C is the heat capacity of the film, d is the thickness of the film, T is the temperature of the superconductor, κ is the thermal conductivity of the film, α is the thermal boundary conductance between the film and the substrate and T_0 is the temperature of the surroundings and the substrate is assumed to be at this temperature as well. The absorption of a photon with energy $\hbar\omega$ results in a temperature increase of $\frac{\hbar\omega\alpha}{4\pi\kappa Cd}$ at that spot. This energy then diffuses outwards with a characteristic distance of $\sqrt{\frac{\kappa d}{\alpha}}$ and a characteristic time scale of $\frac{Cd}{\alpha}$ [18].

Next, the order parameter evolves according to the time-dependent GL equation with the result depending on the bias current [37]. If the current is far away from the critical current, the hot spot will dissipate away and the order parameter recovers to its original value. Thus, no non-superconducting band is formed and the photon is not detected. On the other hand, if the current is close enough to the critical current, the hotspot produces pairs of smaller non-superconducting region called vortex-antivortex pairs. These are named due to the way the superconducting region flows around them. The flow of superconducting current breaks the vortex-antivortex pair apart and forces them to move in opposite direction towards the edge of the detector. This movement causes the superconductor to heat up due to joule heating and results in a non-superconducting band. The resistance of the band reduces the current flow across the detector and forces the excess current to get reflected back. The reflected current is then read out and used as the detector response. This also explains why our microbridge detector has a small active area, as outside of this region the current density is not large enough for the normal band to form.

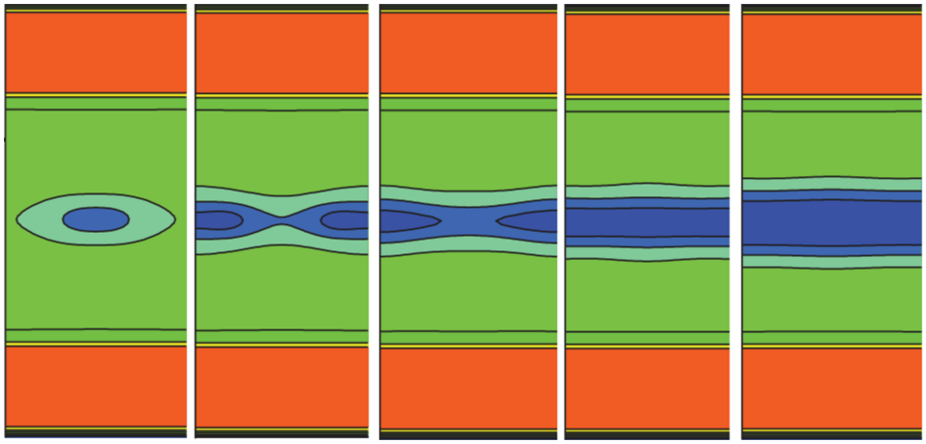

Figure 2.5: Growth of hotspot into non-superconducting band, with time increasing from left to right. Blue indicates regions with suppressed order parameter, green indicates superconducting regions and orange indicates electrical contacts. Figure taken from [37].

Lastly, for the detector to recover to its photon detecting state, it needs to dissipate the heat from the photon absorption and from the joule heating from the current across it. Cooling of the detector is mediated by phonon-electron and phonon-phonon interactions which transfer the heat to the substrate [18]. Note that this dissipation is happening together with the above processes. The resistance of the nanowire in its non-superconducting state is on the order of $10^4\,\Omega$ while for the microbridge, it is on the order of $10\,\Omega$. This results in a larger current and more heat which will cause the microbridge to latch to its non-superconductive state and be insensitive to incoming photons. To reduce the current, a shunt resistor on the order of $1\,\Omega$ is placed is parallel with the detector. After the detector cools, its resistance decreases and the current across it rises back to initial level before the photon absorption. Now, it is ready to detect photons again.

The time scale for the above processes can be understood if we model the detector as a variable resistor and inductor [2, 24]. The resistance is 0 before photon absorption and rises to R_{det} after photon detection. The inductance is L_{k}, which is the kinetic inductance of the detector that depends on the detector material and geometry. Upon photon absorption, the detector forms an LR circuit which enforces a time constant of $\tau_1 = \frac{L_\mathrm{k}}{R_\mathrm{det}}$ on the decay of the current across the detector. After that, the rise of the current back to I_bias has a time constant of $\tau_2 = L_\mathrm{k}\left(\frac{1}{R_\mathrm{shunt}} + \frac{1}{R_\mathrm{trans}}\right)$ for the microbridge and $\tau_2 = \frac{L_\mathrm{k}}{R_\mathrm{trans}}$ for the nanowire. This can be used to give an approximate recovery time of around $\tau_1 + \tau_2$ for the detector and is chosen to be longer than the time taken for the detector to cool down to prevent latching to its non-superconducting state [1].

Chapter 3

Coupling light to microbridge detector

One way to improve the detection efficiency is to have good coupling efficiency. In our setup, this means improving the coupling between an optical fiber and our microbridge detector. In this chapter, I will introduce the beam profile from a fiber followed by the methods we employed to couple light from the fiber to the detector.

3.1 Gaussian beam profile

The light exiting a single mode fiber is described by a Bessel function, but in most cases it can be well approximated by a Gaussian beam [21]. The Gaussian beam intensity profile is given by,

$$I\left(r,z\right) = I_0 \left(\frac{w_0}{w(z)}\right)^2 \exp\left(\frac{-2r^2}{w(z)^2}\right) \ , \tag{3.1}$$

where r is the radial distance from the beam axis, z is the distance from the beam waist along the beam axis, I_0 is the intensity at the center of the beam at its beam waist, w_0 is called the beam waist, and $w(z) = w_0\sqrt{1+\left(\frac{z\lambda}{\pi w_0^2 n}\right)^2}$ is called the beam width, the distance where the intensity falls to e^{-2} of its value at the beam axis. For light exiting a fiber, the beam waist is located at the fiber tip and is given by half of its mode field diameter. For our fiber, SMF-28, this is 10.4 µm at 1550 nm and is already more than double the active area of the detector [33]. Thus, as the beam width will only increase with distance from the fiber, it is crucial to reduce the distance between the fiber tip and detector to maximize the coupling efficiency.

3.2 Zircona sleeve coupling

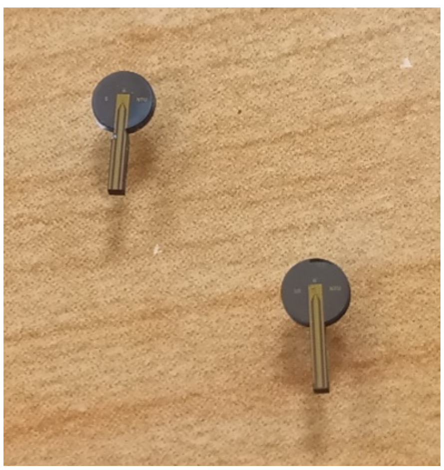

Figure 3.1: Silicon wafer cut into lollipop shape. Detector is located roughly in the center of the circle.

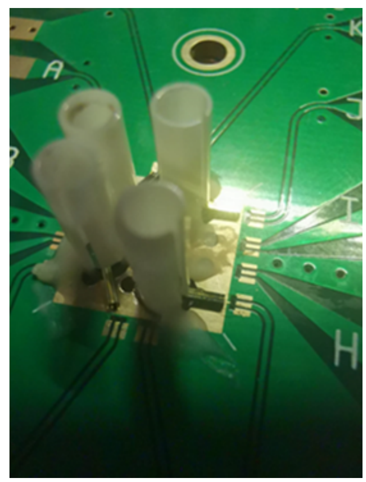

Figure 3.2: Lollipop structure together with white zirconia sleeve epoxied on a PCB.

One of the method used involved laser cutting the silicon wafer into a lollipop shape and using a zirconia sleeve to align the fiber and detector together [22]. This method was chosen due to the tight tolerance between the different components and the low thermal expansion coefficient of zirconia. This allows the different components to remain aligned even when cooled to cryogenic temperatures. However, this tolerance also means a considerable amount of force is required for assembly. Since this was hand assembled, it limits how close the fiber can be brought to the detector. The closest we managed to achieve is around 1 mm which corresponds to a beam width of around 100 µm. This means that only 1 % of light would fall on the active area of the detector. The corresponding system detection efficiency measured was only around 10^{-5} % which is impractical for use in measurements. In addition, the laser cutting process has a high chance of damaging the detector. As such, we have temporarily stopped using this method. Nonetheless, this is still an easy way to package these detectors in a convenient form. Thus, we are currently searching for a more effective way to cut and assemble before resuming this method.

3.3 Cryogenic translation stage

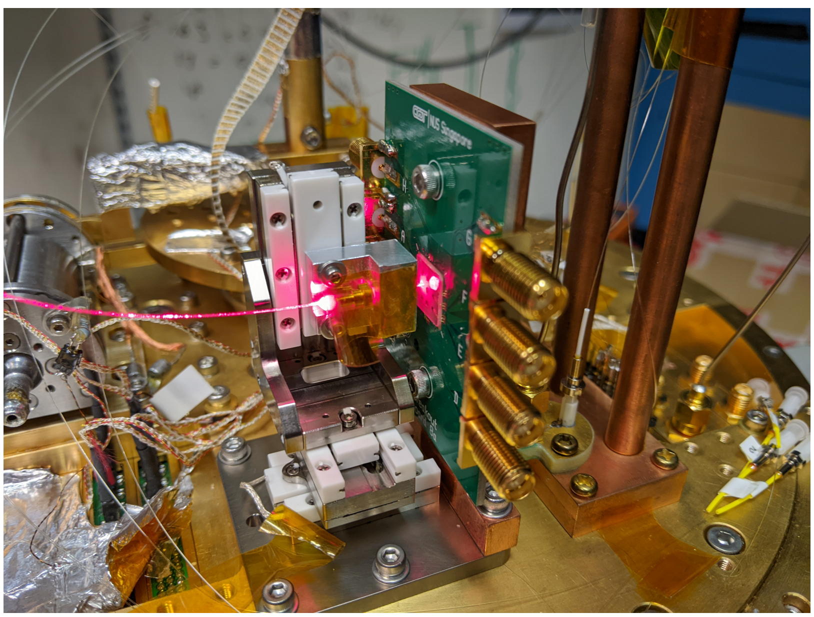

Figure 3.3: Cryogenic translation stage used to position optical fiber. A visible red laser is being used here to perform the rough alignment. The small square on the PCB is the silicon wafer with the detectors.

The current method used in our setup involves a 3-axis cryogenic translation stage to position the optical fiber close to the detector, with the silicon wafer epoxied onto a PCB. This stage is controlled with the attached controller or manufacturer provided code. A small piece of machined aluminum is used to mount the fiber on the detector and the fiber is self terminated with a short section of bare fiber sticking out of the ferrule.

Alignment of the fiber and detector is done in three steps. First, a rough alignment is performed when the fridge is opened by shinning a laser through the fiber and observing the laser spot on the silicon wafer. After closing and cooling the fridge, fine alignment can be done by scanning an area while observing for peaks in the detector count rate. The final alignment is then performed by moving in small steps while observing the count rate.

3.4 Tapered fiber and gradient-index lens

We also explored replacing the optical fiber with a tapered fiber or gradient-index (GRIN) lens to improve the coupling efficiency.

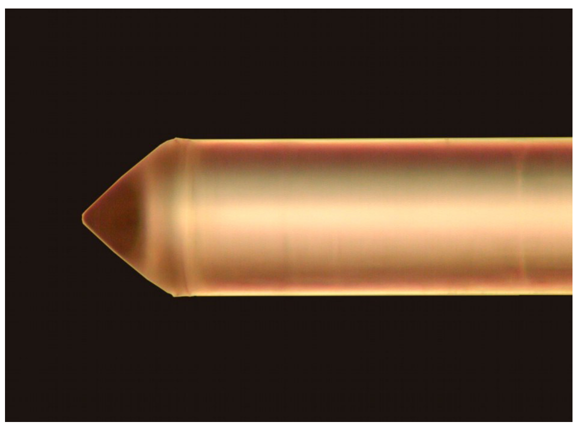

Figure 3.4: Tapered fiber tip. Figure taken from [26]

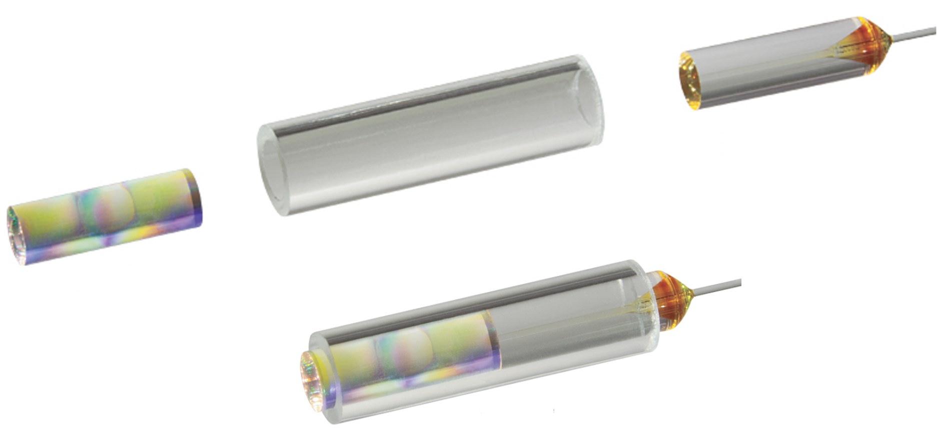

Figure 3.5: GRIN lens components and assembled device. Components from left to right are the GRIN lens, glass mating sleeve and pigtail ferrule. Figure taken from [32]

The tapered fiber is a SMF-28 fiber with its tip shaped to produce a Gaussian beam of beam waist of 2 µm at a distance of 11 µm from the fiber tip for 1550 nm light.

The GRIN lens is a cylindrical glass piece with a varying refractive index in the radial direction given by,

$$n(r) = n_0 \left(1 - \frac{(r\sqrt{A})^2}{2}\right) , \tag{3.2}$$

where n_0 is the refractive index along the optical axis and $\sqrt{A}$ is called the gradient constant. This varying refractive index causes light to refract as it travels through the lens producing a focusing effect. The GRIN lens assembly consist of a fiber connected to a pigtail ferrule, a glass mating sleeve and the GRIN lens. By adjusting the distance between the ferrule and lens, the beam waist and waist position of the output beam can be varied. Calculation for the output Gaussian beam was done using ray transfer matrix analysis with the GRIN lens matrix given by,

$$\begin{pmatrix} \cos\left(l\sqrt{A}\right) & \frac{\sin\left(l\sqrt{A}\right)}{n_0\sqrt{A}} \\ -n_0\sqrt{A}\sin\left(l\sqrt{A}\right) & \cos\left(l\sqrt{A}\right) \end{pmatrix} , \tag{3.3}$$

where l is the length of the GRIN lens [7]. This calculation gives a trend where increasing the distance between the ferrule and the lens decreases the beam waist and the distance between the waist position and the lens, with no lower bound on the possible beam waist. However, this analysis does not take into account diffraction effects and is only applicable in the paraxial regime. Nevertheless, it is still useful as it suggests that we should maximize the distance between the ferrule and lens to achieve a small beam waist.

Before implementing these in our setup, we need to characterize them first. As the beam widths of the beams produced by the GRIN lens and tapered fiber is smaller or comparable to the pixel size of the camera in our lab (3.75 µm), measurements need to be done using the knife-edge technique [5]. In this, a knife-edge such as a razor blade is used to progressively uncover part of the beam while the power transmitted is measured. The power transmitted will follow an error function and can be fitted to deduce its beam width and then reconstruct the beam intensity profile.

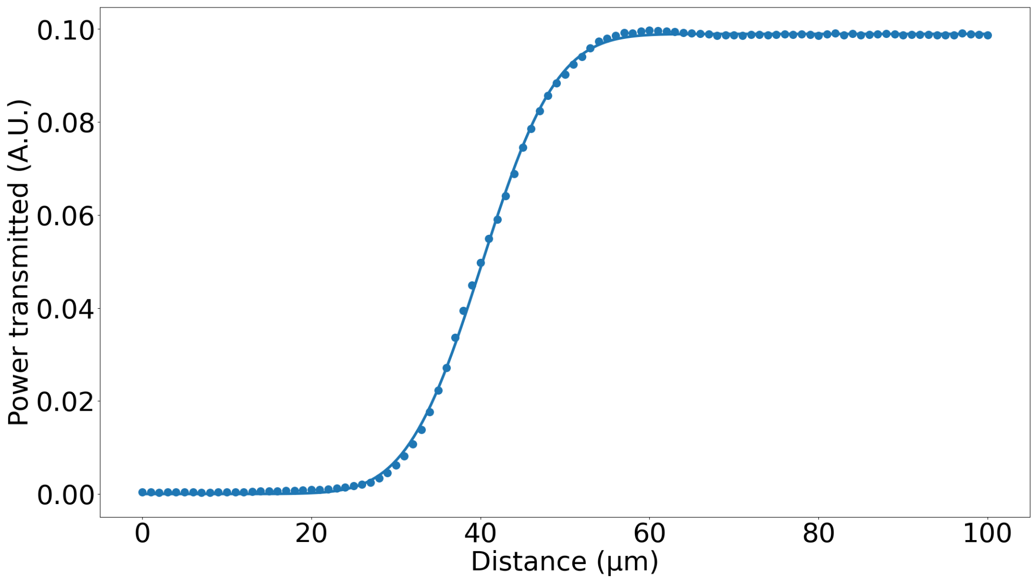

Figure 3.6: Example of knife-edge measurement for tapered fiber. Measured beam width of 13.1(1) μm

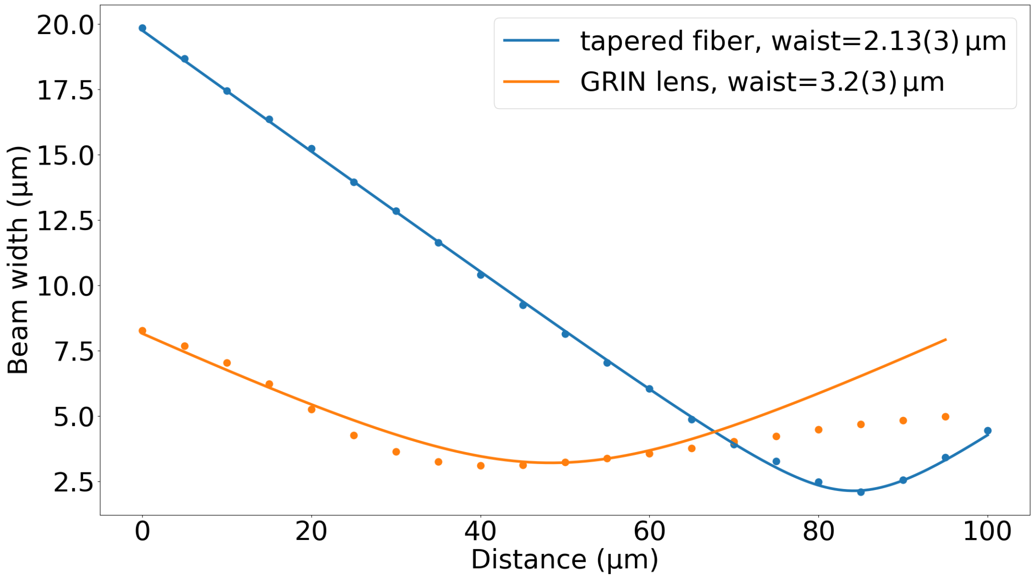

Figure 3.7: Beam profiles of tapered fiber and GRIN lens.

From these measurements the tapered fiber (OZ optics TSMJ-X-1550-9/125-0.25-7-2-12-2-AR) and GRIN lens (Thorlabs GRIN2913) was measured to have a beam waist of 2.13(4) µm and 3.2(3) µm, respectively. We see that the GRIN lens beam profile diverges significantly from an ideal Gaussian profile. One reason for this could be due to the lens and the ferrule being epoxied close the edge of the glass sleeve. This could result in a less mechanically stable assembly than designed leading to a slight misalignment between the optical axis of the ferrule and lens.

Chapter 4

Photon pair generation and detection

Two commonly used light sources in testing of single photon detectors are pulsed lasers attenuated to the single photon level or photon pair sources. For our setup, we used a photon pair source based on spontaneous parametric down conversion (SPDC), a non-linear optical process used to produce tightly time-correlated photon pairs from a more energetic single photon.

4.1 Non-linear optics

Non-linear optics deal with optical processes where the polarization induced in the medium varies non-linearly with the electric field. In general, the polarization can be expanded into a power series in the electric field strength as,

$$\begin{aligned} P(t) &= \epsilon_0[\chi^{(1)}E(t) + \chi^{(2)}E(t)^2 + \chi^{(3)}E(t)^3 + \cdots] \\ &= P^{(1)}(t) + P^{(2)}(t) + P^{(3)}(t) + \cdots \ , \end{aligned} \tag{4.1}$$

where P is the polarization, ϵ_0 is the vacuum permittivity, E is the electric field strength, and χ is the electric susceptibility. We have described these quantities as scalar here but more accurately, P and E are vectors and $\chi^{(n)}$ are tensors of rank $n+1$.

Qualitatively, this non-linear response will produce polarization frequencies that are different from the input electric field frequencies and since polarization is the displacement of charges in the medium and charges with non-zero acceleration radiates EM waves. This results in the production of radiation at frequencies different from the input frequency.

As we are interested in SPDC, we need to look at the second order non-linear polarization $P^{(2)}(t)$. Suppose we have two input fields, one at frequency ω and another at frequency ω_0, with $\omega > \omega_0$ the electric field and the resultant polarization in the medium will be given by,

$$E(t) = E_\omega e^{-i\omega t} + E_{\omega_0} e^{-i\omega_0 t} + \text{c.c} \ , \tag{4.2}$$

$$\begin{aligned} P(t) = {} & \epsilon_0 \chi^{(2)} \left[E_\omega^2 e^{-i2\omega t} + E_{\omega_0}^2 e^{-i2\omega_0 t} + 2E_\omega E_{\omega_0} e^{-i(\omega+\omega_0)t} + 2E_\omega E_{\omega_0}^* e^{-i(\omega-\omega_0)} + \text{c.c} \right] \\ & + \epsilon_0 \chi^{(2)} \left[2|E_\omega|^2 + 2|E_{\omega_0}|^2 \right] \ , \end{aligned} \tag{4.3}$$

where c.c. means complex conjugate. The fields and polarization are described in complex notation here for ease of manipulation but since they are physical quantities, they are real.

We can identify the polarization terms at different frequencies with their respective different non-linear processes. The components at 2ω and $2\omega_0$ are responsible for second harmonic generation where two photons of the same frequency combine to form a photon with twice the frequency. The components at $\omega+\omega_0$ and $\omega-\omega_0$ are responsible for sum-frequency generation and difference-frequency generation, respectively. Sum-frequency generation is the same as second harmonic generation, just with two photons of different energies. However, difference-frequency generation is different since the more energetic photon is split into two photons, one with frequency $\omega-\omega_0$ and another with frequency ω_0. This can be thought of amplifying the initial input field. The last two non-oscillating terms are responsible for optical rectification, which is just a fixed displacement of the charges equilibrium position.

Note that none of the terms in the above expression can be used to explained SPDC directly, since none of them corresponds to one photon at ω splitting into two photons at ω_0 and $\omega - \omega_0$ without the presence of the beam at ω_0. But if we quantize the electromagnetic field and let the vacuum field to be our ω_0 field, we can explain SPDC as difference-frequency generation. This lets us view SPDC and difference-frequency generation as the spontaneous and stimulated analogues of each other. Although SPDC is a quantum process, this classical description of non-linear optics is useful in gaining some intuition about SPDC. The proper quantum description of SPDC is out of the scope of this thesis but interested readers may refer to [13] for a basic introduction where SPDC is introduced as a means to produce squeezed states.

Despite the above example suggesting that many different outputs are possible, there is usually only one dominant process due to the phase matching condition. This applies for both classical and quantum processes.

From the next section onward, we will concern ourselves only with SPDC and difference-frequency generation. We also introduce the convention found in literature, where ω is called the pump frequency, ω_0 the signal frequency and $\omega - \omega_0$ the idler frequency. Subscripts will be used to distinguish between the different frequencies.

4.2 Phase matching

To derive the phase matching conditions, we need to solve the electromagnetic wave equation in matter. However, this is beyond the scope of this thesis but the details can be found in [4]. From this, we get the following expression for the intensity of the idler beam,

$$I = \frac{8 d_{\text{eff}}^2 \omega_i^2 I_p^2 I_s^2}{n_{\omega_p} n_{\omega_s} n_{\omega_i} \epsilon_0 c^3} L^2 \text{sinc}^2(\frac{\Delta k L}{2}) = I_{\text{max}} \text{sinc}^2(\frac{\Delta k L}{2}) \ , \tag{4.4}$$

where d_{eff} is the effective non-linear coefficient which depends on χ, the polarization of the input beams and the angle between the input beams and the optical axis, I is the intensity of the input beams, n is the refractive index of the medium, L is the length of the medium traveled, k is the wave vector, $\Delta k = k_p + k_s - k_i$ is the phase mismatch, and $L_{\text{coh}} = \frac{\pi}{\Delta k}$ is called the coherence length.

From this equation and the graph below, we can see that if $\Delta k \neq 0$ the intensity of the idler beam oscillates as the energy oscillates between the pump beam and the signal and idler beams. When $\Delta k = 0$ the intensity of the idler beam grows quadratically. The quantum nature of SPDC is also apparent here, since with the absence of the signal beam, $I_s = 0$, there will be no idler beam at all.

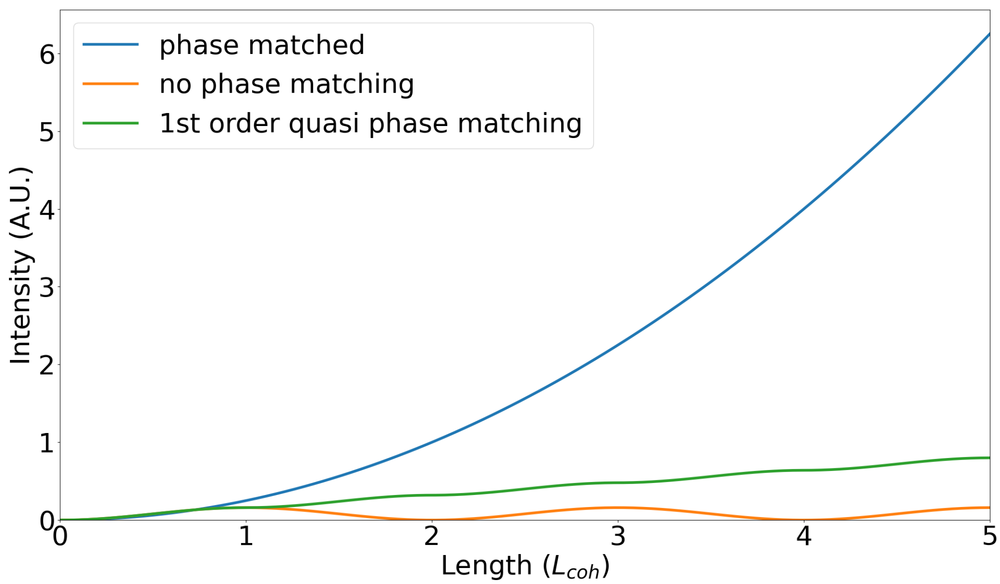

Figure 4.1: Intensity of idler beam vs length of crystal for different phase matching conditions

It is clear that we want to achieve $\Delta k = 0$, where the three beams are phase matched. However, most transparent medium display normal dispersion in the visible spectral region, where normal dispersion is defined as,

$$\frac{\mathrm{d}n}{\mathrm{d}\lambda} < 0 \ . \tag{4.5}$$

This means that the three beams will travel at different speeds in the medium, making it difficult to fulfill the phase matching condition. To solve this, we could use a birefringent material with different refractive index curves for its different optical axes. The phase matching condition can then be fulfilled by choosing different polarizations for the three beams. The refractive index is given by the empirical Smellier equation,

$$n_{\mathrm{i}}^2 = A_{\mathrm{i}} + \frac{B_{\mathrm{i}}}{1 - \frac{C_{\mathrm{i}}}{\lambda^2}} + \frac{D_{\mathrm{i}}}{1 - \frac{E_{\mathrm{i}}}{\lambda^2}} - F_i \lambda^2 \ , \tag{4.6}$$

where i is an index labeling the directions relative to the optical axis, one parallel and two orthogonal to the axis and each other. A, B, C, D, E and F are constants that are found experimentally. For our crystal, potassium titanyl phosphate (KTP), they can be found in [10, 12].

In addition to this, it is also possible to temperature tune the crystal to achieve better phase matching. This is done by considering the change in refractive index due to temperature which for KTP was found to follow an empirical equation given by,

$$\Delta n = n_1(T - 25) + n_2(T - 25) \ , \tag{4.7}$$

$$n_{1,2} = \sum_{m=0}^{3} \frac{a_m}{\lambda^m} \ , \tag{4.8}$$

where T is the temperature in degree Celsius and a are constants that are found experimentally. We used the values found in [9] to calculate the temperature dependence at our photon pair wavelengths.

However, a crystal birefringence may not be enough to fulfill the phase matching condition for certain wavelengths. Thus, the quasi phase matching technique was created as a means to compensate for the phase mismatch. In this method, the crystal axes of the medium orthogonal to the direction of propagation is periodically inverted with a poling period, Λ, such that the crystal axis is inverted every $\frac{\Lambda}{2}$. Doing so reverses the flow of energy from the output fields to the input field, allowing us to continually pump energy into the output fields. Following the calculations found in [4], the phase mismatch is modified to,

$$\Delta k = k_p + k_s - k_i + \frac{2\pi m}{\Lambda} , \tag{4.9}$$

where m is the order of the quasi-phase matching which is typically $m = 1$ as it results in highest intensity. For 1st order quasi-phase matching, the poling period is,

$$\Lambda = \frac{2\pi}{k_p + k_s - k_i} = 2L_{\mathrm{coh}} . \tag{4.10}$$

Additionally, we also need to take into account the thermal expansion of the crystal in the calculation for the poling period,

$$\Delta l = l[1 + \alpha\,(T - 25)] , \tag{4.11}$$

where α is the linear thermal expansion coefficient in the propagation direction and can be found in [25] for KTP.

The different phase matching schemes lets us classify the SPDC process as type-0, type-I , or type-II. In type-0, the pump, signal and idler beams all have the same polarization, in type-I, the signal and idler beams have the same polarization orthogonal to the pump beams, and in type-II, the signal and idler beams have orthogonal polarization.

4.3 Detection scheme for photon pairs

The detection of the photon pairs is done using a pair of single photon detectors, but in addition to the counts due to the photon pairs produced by the source, there are also dark counts from the detectors themselves. To distinguish between them, we need to perform a coincidence measurement with the two detectors, where one of the photon will be used to herald the presence of the other photon.

A simple setup for this can be done like so. The photon pairs from the source is split using a beam splitter and sent to the detectors. Naming the heralding detector 1 and the heralded detector 2, both detectors output are then sent to an AND gate, with detector 2 having a delay, t_d, relative to detector 1. The output from detector 1 is used to start a coincidence window of length τ centered at t_d. τ is mainly determined by detector timing jitter as the photon pairs from are tightly time correlated ($< 1\,\mathrm{ps}$) [16]. If detector 2 detects a photon within this window, this means that a photon pair is detected and a signal pulse is produced by the AND gate.

In our setup, this is done digitally, where the AND gate is replaced with a timestamp card which records the detector output timings to a computer and a cross correlation function. The cross correlation for two discrete time series is,

$$D_1 \star D_2[T] = \sum_{t=0} D_1(t) D_2(t+T) \ , \tag{4.12}$$

where $D_{1,2}$ are the discrete photon detection time tags and T is the delay between the two time series. The output from this will then be the number of times detector 2 detect a photon at $t+T$ when detector 1 detects a photon at t. We would expect a peak around t_d and this is illustrated with an example below.

Detector 1 time tags (ns)	6	8	14	30	44	52	66	70	74	88
Detector 2 time tags (ns)	14	16	28	34	54	60	78	80	82	96

Time delay (ns)	2	4	6	8	10	12	14	16	18	20
Cross correlation	0	1	0	5	2	0	2	0	0	0

Table 4.1: Example of detection from time tags using a 2 ns time stamp card and the corresponding cross correlation.

From the above data, we see a peak at around 8 ns, which indicates that t_d is around 8 ns. Then, if we use a coincidence window of 6 ns from 6 ns to 12 ns, we sum up all coincidences at 6, 8 and 10 ns to get the number of pairs detected which is 7 is this example.

Next, we need to remove the accidental coincidences from this number. Unfortunately, there is no way to distinguish between actual pairs and accidental coincidences, so we have to rely on a commonly used approximation as follow. Suppose we count the number of pairs over an integration time, $\mathcal{T}$, and the detection rate of both detectors are $s_1\,\mathrm{s}^{-1}$ and $s_2\,\mathrm{s}^{-1}$ respectively. The total time that the coincidence window is open for is $s_1 \times \tau$. Then, assuming that detector 2 counts are uniformly distributed over the integration time, the number of accidentals is,

$$\text{accidentals} = s_1 \times s_2 \times \tau \times \mathcal{T} \ . \tag{4.13}$$

This scheme also allows us to characterize the source by its heralding efficiency, the probability of detecting a 2nd photon conditional on detecting the heralding photon. This is defined as,

$$\eta = \frac{p}{\sqrt{s_1 \times s_2}} \ , \tag{4.14}$$

where p is the pair rate.

4.4 Source calculations and construction

In this work, a 1 cm long periodically poled potassium titanyl phosphate (PPKTP) crystal is used to built a type-0 source degenerate around 1560 nm. A pump laser at 780 nm is used to satisfy the conservation of energy while a poling period of 24.97 µm was chosen to meet the phase matching condition at around 50 °C. In the conceptual introduction, all light was in the form on plane waves but in practice, the light is more accurately described in the basis of Gaussian spatial modes. To account for this, we used the Bennink model [3]. Optimizing for the collection efficiency, we ended up with a pump beam waist of 100 µm and an output beam waist of 80 µm to achieve a theoretical collection efficiency of 93 %.

For the pump laser, we used a external cavity diode laser in a Littrow configuration, where an external grating is used to form the cavity. The resonant wavelength is then chosen by tuning the angle of the grating as well as temperature tuning the laser diode (Thorlabs L785H1) through a proportional-integral-derivative (PID) controller. Using a spectrometer, we measured the following spectrum for the laser.

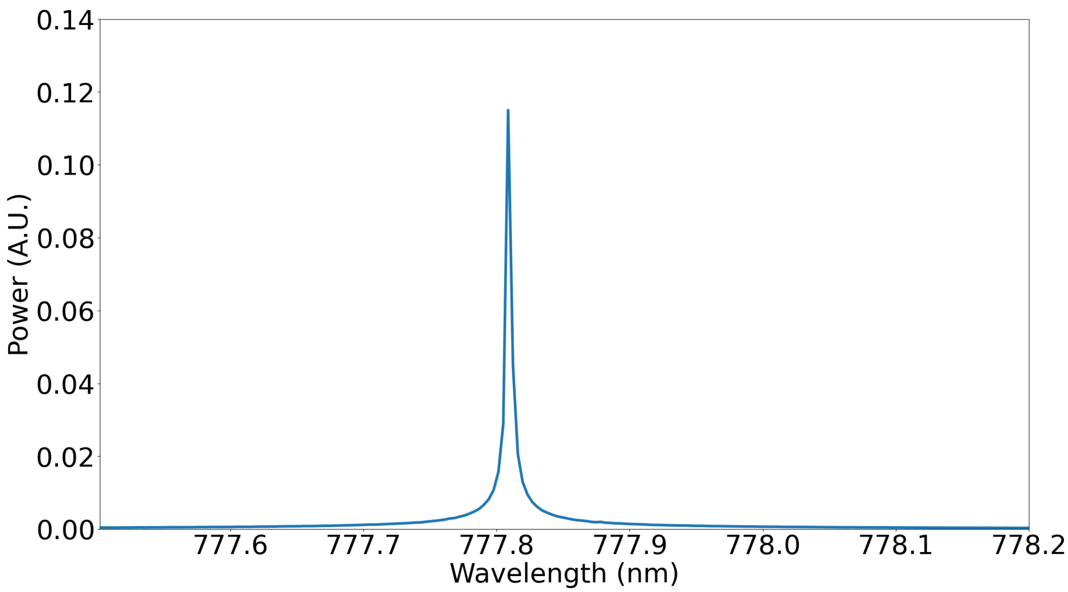

Figure 4.2: Spectrum of pump laser peaking at 777.81 nm.

The light is then carried to the source using a fiber placed inside a fiber polarization controller (Thorlabs FPC560) which acts as a combination of quarter wave plate (QWP), half wave plate (HWP) and another QWP. These 3 optical elements together with the polarizing beam splitter (PBS) and HWP in the source will be sufficient to create any linear polarization of light (vertical for our type-0 SPDC process) to maximize the pair rate.

Next, the light enters the source through a fiber launcher which is used to couple light into free space and vice versa using an aspheric lens. By controlling the distance between the lens and fiber in the launcher we are able to control the beam size in free space. To measure the pump beam waist, a CMOS camera was used to image the beam along the optical axis and a 2D Gaussian was fitted to the images to get the beam width along the beam axis. These widths were then fitted to acquire the beam waist. For the output beam, we tried shining a

1560 nm laser from the collection launcher and imaging that but this wavelength was outside of the spectral response range of the camera. As such, we calculated the equivalent beam waist for a 1310 nm laser with the same optics and measured that instead.

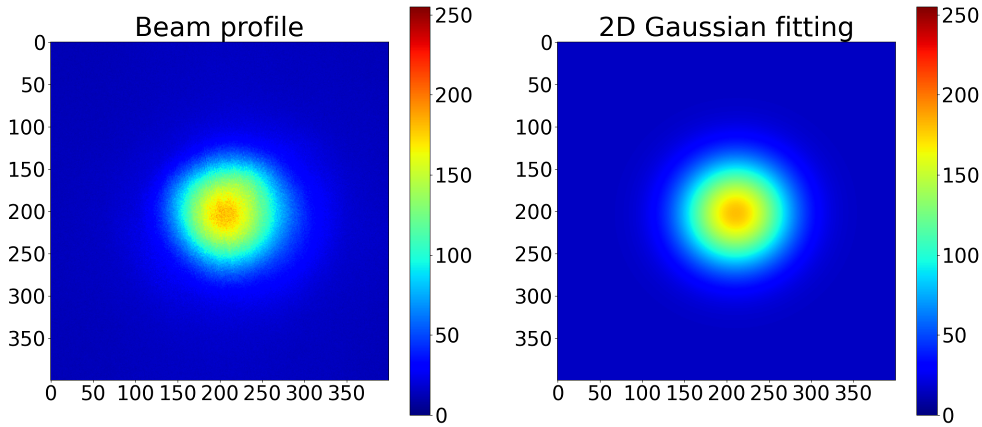

Figure 4.3: Image of a 1310 nm beam and the fitted 2D Gaussian. Units on axes correspond to pixel number with each square pixel having a dimension of 3.75 µm. Color is proportional to intensity of light on the pixel. This image gives a fitted beam waist of around 330 µm.

Now, the PPKTP is placed in the source with the temperature tuning done using an oven attached to a PID controller. A long pass filter (Thorlabs FELH 1350) is also placed after the crystal to remove any remaining pump light before it enters the collection fiber.

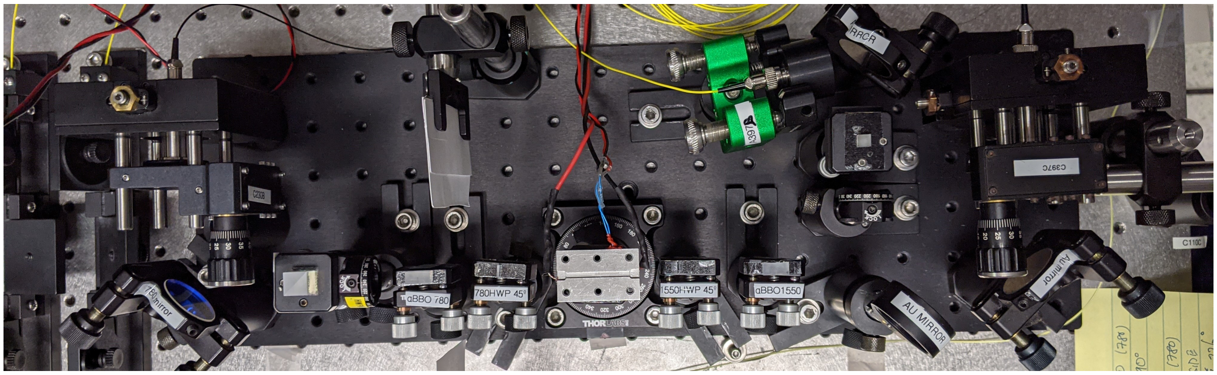

Figure 4.4: Image of source built. Light enters from the left launcher and exits from the right launcher. In order from left to right, the elements that the 780 nm light passes through are, mirror, PBS, HWP in a rotating mount, α-BBO, HWP, PPKTP in oven, HWP, α-BBO, mirror, and long pass filter which is hidden by the fiber launcher. The purpose of the α-BBO and additional HWP will be covered in the next chapter.

4.5 Source measurements

To measure the source parameters, we split the light from the source using a 50:50 fiber coupler and send it to 2 InGaAs SPADs with detection efficiency of around 10%. Without accounting for the detector efficiency and the splitting of the light, we measured a pair rate of around $10^3\,\mathrm{pairs\,s^{-1}\,mW^{-1}}$ and a count rate of $8.5 \times 10^4\,\mathrm{counts\,s^{-1}\,mW^{-1}}$ and $9.2 \times 10^4\,\mathrm{counts\,s^{-1}\,mW^{-1}}$. Corresponding to a heralding efficiency of 1.09 %. If we correct for the efficiency of the detectors and the splitting of the pairs using a 50:50 fiber coupler, this increases to a pair rate of $4 \times 10^4\,\mathrm{pairs\,s^{-1}\,mW^{-1}}$ and heralding efficiency of 43.6 %.

We also measured the spectrum of the source by sending the light from the source to a grating spectrometer followed by an InGaAs SPAD. By measuring the counts for different angles of the grating corresponding to different wavelengths, we measured the following spectrum.

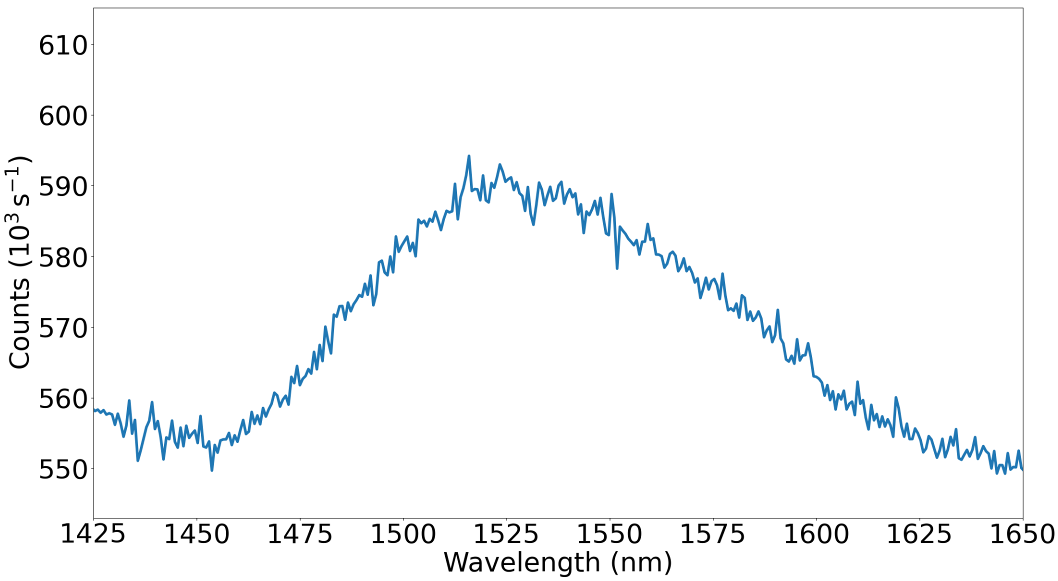

Figure 4.5: Spectrum of pair source with peak around 1525 nm.

From energy conservation, we should expect a peak around 1556 nm instead. The shift in the peak could be attributed to the grating used in the spectrometer (GR25-0613) which has a non-uniform efficiency in this wavelength range which affects the shape of the spectrum.

Chapter 5

Entanglement of photon pairs

With some modifications, the photon pair source is easily upgraded to a polarization entangled photon pair source. This allows it to be used for other experiments such as quantum key distribution using the E91 or BBM92 protocols.

5.1 Entangled pair source configuration

The configuration used is a linear beam-displacement interferometer where birefringent α-barium borate (BBO) is used to separate and combine the pump and output beams [11]. The additional optics used to convert the pair source into an entangled pair source are the two sets of BBO and HWP that are placed before and after the crystal. Besides that, the HWP after the PBS was also rotated to produce diagonally polarized light such that there is equal power in both beams.

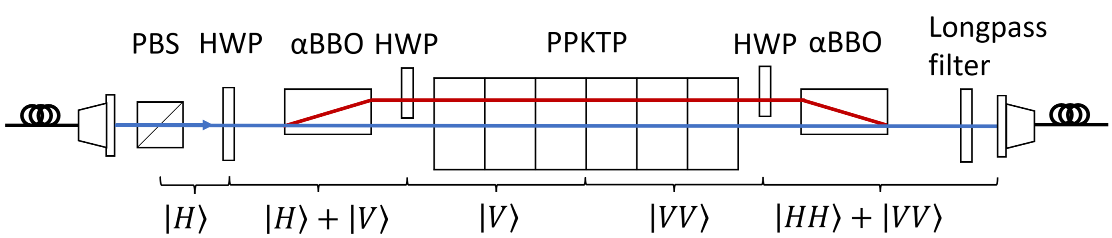

Figure 5.1: Schematic of the entangled pair source with the states at the different parts of the source labelled

To see why the state produced by this source is an entangled state, we follow the polarization changes in the source. The diagonally polarized light is first split into two beams with a separation of 1 mm by the BBO. The top path contains $|H\rangle$ and the bottom contains $|V\rangle$. The light in the top path is rotated into $|V\rangle$ by a HWP and SPDC converts both paths to $|VV\rangle$. Another HWP in the top path rotates the state into $|HH\rangle$ which allows it to recombine with the $|VV\rangle$ beam using the BBO. Now, if we were to take a photon pair from the combined beam, it will be impossible to distinguish which beam the pair came from. Thus, we can write it as,

$$\frac{1}{\sqrt{2}}\left[|HH\rangle + e^{-i\phi}|VV\rangle\right] \ , \tag{5.1}$$

where ϕ is the phase difference due to the different path lengths. Setting this to even or odd multiples of π will give us the Bell states $|\Psi^{+}\rangle$ or $|\Psi^{-}\rangle$ respectively. This can be done through manipulating the angle of the HWP with respect to the beam, or introducing an optical delay in the form of a piece of glass.

5.2 Quality of entanglement

A commonly used metric for the quality of entanglement is the visibility of the source, which is the joint detection probability for a measurement basis. This is done by introducing a polarizer before each detector in the coincidence measurement setup. Each polarizer consist of a HWP followed by a PBS. The PBS projects the light onto $|H\rangle$ and the HWP can be used to rotate any linearly polarized light into $|H\rangle$. Measuring the visibility in the H/V basis can be done by first fixing one of the polarizer to project onto $|H\rangle$ or $|V\rangle$, but we'll use $|H\rangle$ in this example. Next, we measure the number of coincidences with the other HWP at different angles corresponding to projection onto different polarization states. Following the derivation using Jones calculus found in [31], the pairs detected as a function of angle of the rotating polarizer will be,

$$p = (p_{\max} - p_{\min}) \sin^2 \theta + p_{\min} \ , \tag{5.2}$$

where $p_{\max,\min}$ is the maximum and minimum number of pairs detected and θ is the angle between the optical axis of the two HWPs. From this, we can define the visibility to be,

$$\mathcal{V} = \frac{p_{\max} - p_{\min}}{p_{\max} + p_{\min}} \ . \tag{5.3}$$

As the photon pairs are given by equation 5.1, the maximum occurs when both polarizer are projecting onto $|H\rangle$ and minimum occurs when the rotating polarizer is projecting onto $|V\rangle$. As such, we can rewrite the visibility as,

$$\mathcal{V}_{H/V} = \frac{p_{HH} - p_{HV}}{p_{HH} + p_{HV}} \ , \tag{5.4}$$

where $p_{HH,HV}$ is the number of pairs when measuring the photon pair in the $|HH\rangle$ and $|HV\rangle$ state respectively. After correcting for accidentals, we should expect this to be close to 1. However, the mixed state $\rho = \frac{1}{2} |HH\rangle \langle HH| + \frac{1}{2} |VV\rangle \langle VV|$ will also yield the same result. To show entanglement, we will need to measure the visibility in the D/A basis as well. For the mixed state, the visibility in the D/A basis would be 0 as the probability of projecting onto $|DD\rangle$ or $|DA\rangle$ is the same. The entangled state would always be non-zero, as it can be written as,

$$\frac{1}{2\sqrt{2}} \left[\left(1 + e^{-i\phi}\right) (|DD\rangle + |AA\rangle) + \left(1 - e^{-i\phi}\right) (|DA\rangle + |AD\rangle) \right] \ . \tag{5.5}$$

This shows how visibility can be used to distinguish between entangled and mixed states. Furthermore, the visibility in the D/A basis can be used to check how close the output state is to $|\Phi^{\pm}\rangle$ as only these states yield a visibility close to 1 for both basis.

5.3 Visibility results

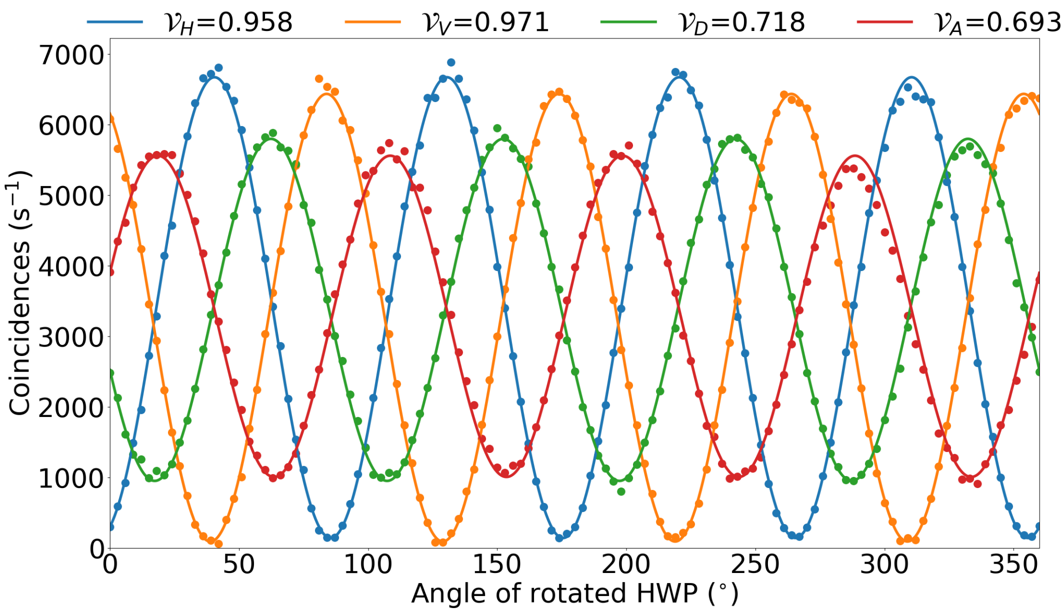

Figure 5.2: Visibility curves and the corresponding visibilities. Rotating polarizer was rotated a full circle. Subscript in visibility indicates the polarization of the fixed polarizer

There are several feature in this plot to unpack. First, measuring the visibility in the H/V basis with the fixed polarizer projecting onto $|H\rangle$ or $|V\rangle$ yields two different peak coincidence values. We suspect that this is due to the $|HH\rangle$ and $|VV\rangle$ beams not overlapping completely after the second BBO. This would result in more $|HH\rangle$ pairs being collected than $|VV\rangle$. One possible means to correct this would be to split the pump beam unequally, with more power going into the $|V\rangle$ beam to compensate for the coincidences. Next, we have a non-zero $\mathcal{V}_{\mathrm{D}}$ and $\mathcal{V}_{\mathrm{A}}$, this means that our source indeed produces entangled pairs. Lastly, the significantly lower visibility for $\mathcal{V}_{\mathrm{D}}$ and $\mathcal{V}_{\mathrm{A}}$ shows that our source does not produce the Bell states.

Chapter 6

Microbridge measurement results

In this chapter, I will go through the various measurement results from the microbridge, the voltage pulse from a photon detection event, the dependence of dark count and efficiency on the bias current, and the timing jitter of the detector.

6.1 Microbridge output pulse

Using an oscilloscope connected to the amplifier in section 2.3 we can measure the voltage pulse of the detector. Our detector voltage pulse has a pulse height of 374 mV and a noise level of 14.5 mV, giving us a signal-to-noise ratio of around 26. The noise jitter is defined as,

$$\text{noise jitter} = V_{\text{n}} \times \frac{\mathrm{d}t}{\mathrm{d}V} \ , \tag{6.1}$$

where V_{n} is the voltage amplitude of the noise and $\frac{\mathrm{d}V}{\mathrm{d}t}$ is the gradient of the rising edge. This can be interpreted as the variation of the rising edge due to the noise and since the counter discriminates on the rising edge, introduces uncertainty as to when the count is registered. For our detector, the noise jitter is around 10 ps.

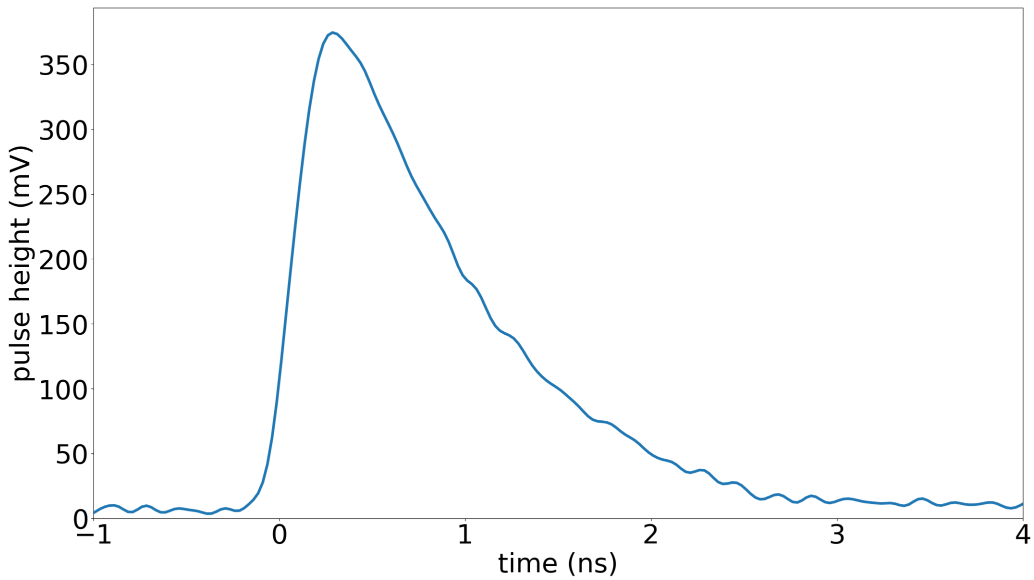

Figure 6.1: Typical voltage pulse output by the detector.

6.2 Dark counts and detection efficiency

Due to thermal fluctuations, non-superconducting bands may form without the presence of light, giving rise to dark counts. Increasing the bias current increases the sensitivity of the transition into its resistive state to thermal fluctuations, increasing the dark count rate. We tested this dependence by measuring the count rate of the detector with no light source attached. Next, to measure the dependence of detection efficiency with bias current, we used a laser diode at a fixed current below its lasing threshold.

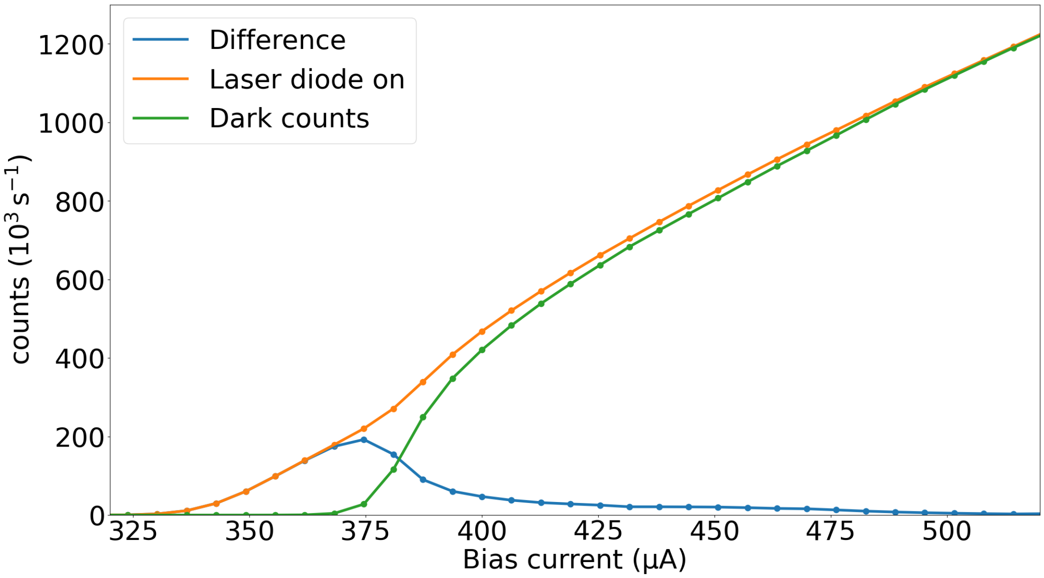

Figure 6.2: Dark count and count rate for different bias currents.

First, we observed the expected increase in dark counts with bias current. Second, as the laser diode current is fixed, the difference in count rate is proportional to the detection efficiency. Increasing the bias current increases the detection efficiency up till a threshold where the dark counts start to dominate. This means that there is an optimal bias current where the detection efficiency is maximized and for this detector, its around 375 μA

6.3 Timing jitter

Measurement of the timing jitters of the detectors is done with the same setup used for detecting photon pairs as described in section 4.3 but in this case, the cross correlation takes another meaning. It is the cross correlation between both detectors instrument response function (IRF), a distribution that describes the timing delay between the photon arrival and the detector response, with the full width half maximum (FWHM) of this distribution typically quoted as the timing jitter of the detector. For timing jitter measurements, one of the detector is a reference detector with a known IRF and timing jitter. Then, performing the deconvolution of the cross correlation with the reference IRF yields the other detector

IRF.

In this work, we make the assumption that both detectors used have IRFs that can be modeled with a Gaussian. This makes it easier to calculate the jitter since the cross correlation is another Gaussian,

$$\begin{aligned} G_1 \star G_2 [T] &= N G_1 (\sigma_1, T) \star G_2 (\sigma_2, T) \\ &= N G \left(\sqrt{\sigma_1^2 + \sigma_2^2}, T \right) \ , \end{aligned} \tag{6.2}$$

where N is the total number of counts detected, σ is the width of the Gaussian which is related to the FWHM by FWHM $= 2\sqrt{2\ln(2)}\sigma$.

Due to the low detection efficiency of the microbridge, we could not use the 1560 nm pair source constructed in the earlier chapters but instead use a bright pair source that produces photons at 586 nm and 1310 nm. The 586 nm photons are sent to the reference detector, a Si APD (Micro Photon Devices PD-050-CTC-FC) which was characterized to have a timing jitter of around 40 ps [30].

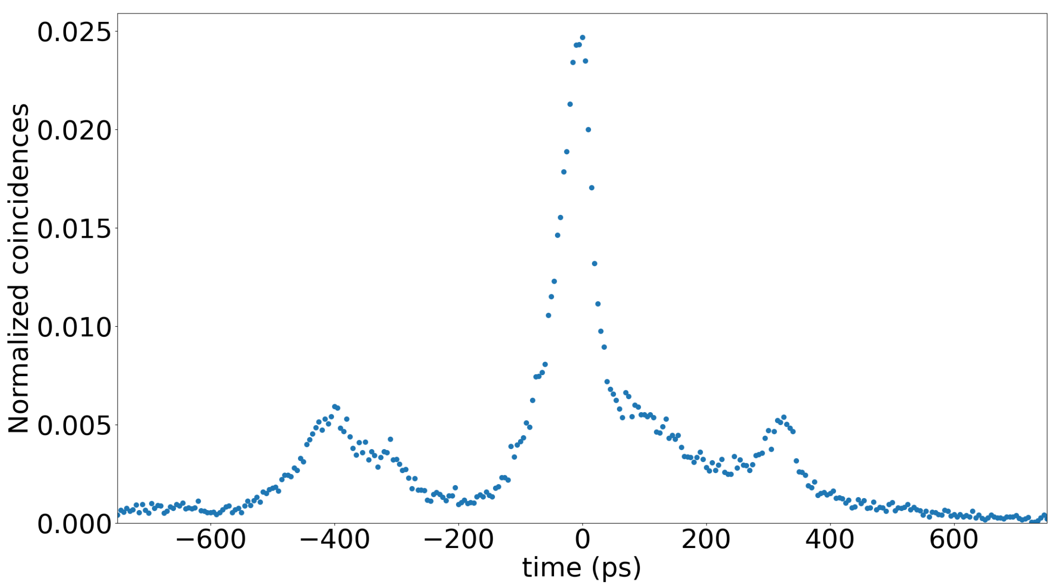

Figure 6.3: Cross correlation between Si APD and microbridge detector. The tail after the main peak is a feature of the IRF of the Si APD.

From the main peak, we can read off that the FWHM is 150 ps which corresponds to a jitter of around 141 ps for our microbridge detector.

An interesting feature is the presence of multiple peaks, suggesting that the detector has several distinct timing responses. Initially, we thought this could be due to a region outside the 2 µm × 2 µm area still having a high enough current density for the normal band formation to take place. Leading to normal bands that are further or closer from the positive contact with reflected current pulses that would take a longer or shorter time to travel back respectively. This would result in several peaks corresponding to different delays. However, we have no reason to suspect that the bands only occur at three distinct regions rather than one continuous region. This leads to us to believe that this could be due to the unevenness of the superconducting layer instead. The unevenness would result in regions with lower critical current density, allowing the formation of a normal band even with increased width. Nonetheless, these are just our speculations and further testing is required for confirmation. Despite this, the timing jitter measurement shows that our detector is single photon sensitive.

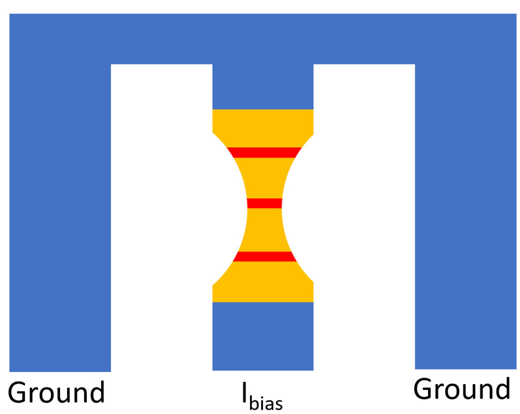

Figure 6.4: Possible spots where the normal bands could form. Blue correspond to the electrical contacts, orange correspond to the microbridge and red corresponds to the normal bands.

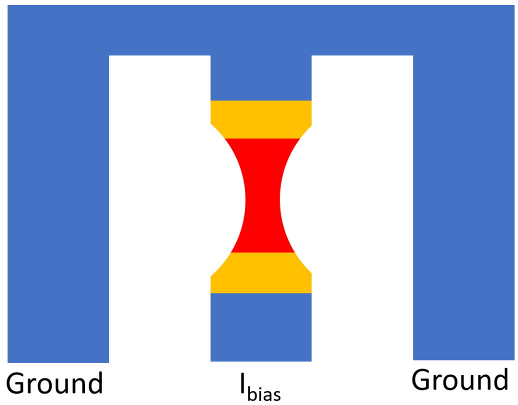

Figure 6.5: Possible region where the normal band could form

Chapter 7

Conclusion and future work

In this thesis, we worked towards the characterization of superconducting microbridge detectors which at this time seems to offer some of the best performance in the infrared region. We started with exploring different methods to couple light onto the small active area of the detector. Initially, we attempted to use a zirconia sleeve to hold the fiber and detector but this was met with a poor success rate. Currently, a 3-axis piezo stage is used to position the fiber achieving a detection efficiency of around 10^{-4} %.

Next, we constructed a 1560 nm pair source to test for the detector single photon response and to characterize it. The source was characterized to have a brightness of around 4×10^5 pairs $\mathrm{s}^{-1}\,\mathrm{mW}^{-1}$ with a heralding efficiency of 43.6 %.

Lastly, we characterized the detector by measuring its output pulse, the dark count and detection efficiency dependence on the bias current, and its timing jitter. From the output pulse, we measured a signal-to-noise ratio of 26 with a corresponding noise jitter of 10 ps. The dark counts and detection efficiency was found to increase with bias current but beyond a certain threshold, the dark counts would start to dominate and decrease the efficiency. The timing jitter of the detector was measured to be around 150 ps. Multiple peaks were also observed in the cross correlation but no definite reason can be provided at this time.

7.1 Future works

7.1.1 Improvements to the entangled pair source

The construction of the pair source is a side goal of this project and is thus in a sub-optimized state. As a source of photon pairs, future works would include tuning the laser to 780 nm and temperature tuning the crystal to maximize the pair rate. As a source of entangled pairs, future works would include balancing the pairs in the $|HH\rangle$ and $|VV\rangle$ beams and optimizing the source to produce $|\Psi^+\rangle$ or $|\Psi^-\rangle$.

7.1.2 Improvements to superconducting microbridge

The immediate next steps in developing the microbridge would be to improve the detection efficiency and to investigate the multiple peaks in the cross correlation in section 6.3. Improving the detection efficiency could be done by improving the alignment of the fiber and detector or using the tapered fiber and GRIN lens in section 3.4. Investigation of the multiple peaks would be done by trying different detector geometries.

7.1.3 High temperature superconducting detectors

A long term goal would be to create and test detectors made out of other superconducting material. An interesting choice would be to use high temperature superconductors to create detectors that could work at liquid nitrogen temperatures. This could potentially make superconducting detectors more widespread compared to current detectors that requires helium to cool.

Bibliography

[1] Anthony J Annunziata, Orlando Quaranta, Daniel F Santavicca, Alessandro Casaburi, Luigi Frunzio, Mikkel Ejrnaes, Michael J Rooks, Roberto Cristiano, Sergio Pagano, Aviad Frydman, et al. Reset dynamics and latching in niobium superconducting nanowire single-photon detectors. *Journal of Applied Physics*, 108(8):084507, 2010.

[2] Claire Autebert, Gaëtan Gras, Emna Amri, Matthieu Perrenoud, Misael Caloz, Hugo Zbinden, and Félix Bussières. Direct measurement of the recovery time of superconducting nanowire single-photon detectors. *Journal of Applied Physics*, 128(7):074504, 2020.

[3] Ryan S. Bennink. Optimal collinear gaussian beams for spontaneous parametric down-conversion. *Phys. Rev. A*, 81:053805, May 2010.

[4] Robert W Boyd. *Nonlinear optics*. Academic press, 2020.

[5] JJ Chapman, BG Norton, EW Streed, and D Kielpinski. An automated submicron beam profiler for characterization of high numerical aperture optics. *The Review of Scientific Instruments*, 79(9):095106–095106, 2008.

[6] John R Clem and Karl K Berggren. Geometry-dependent critical currents in superconducting nanocircuits. *Physical Review B*, 84(17):174510, 2011.

[7] Jay N Damask. *Polarization optics in telecommunications*, volume 101. Springer Science & Business Media, 2004.

[8] Matthew D Eisaman, Jingyun Fan, Alan Migdall, and Sergey V Polyakov. Invited review article: Single-photon sources and detectors. *Review of scientific instruments*,

82(7):071101, 2011.

[9] Shai Emanueli and Ady Arie. Temperature-dependent dispersion equations for ktiopo 4 and ktioaso 4. *Applied optics*, 42(33):6661–6665, 2003.

[10] Tso Yee Fan, CE Huang, BQ Hu, Roger C Eckardt, YX Fan, Robert L Byer, and RS Feigelson. Second harmonic generation and accurate index of refraction measurements in flux-grown ktiopo 4. *Applied optics*, 26(12):2390–2394, 1987.

[11] Marco Fiorentino and Raymond G. Beausoleil. Compact sources of polarization-entangled photons. *Opt. Express*, 16(24):20149–20156, Nov 2008.

[12] K Fradkin, A Arie, A Skliar, and G Rosenman. Tunable midinfrared source by difference frequency generation in bulk periodically poled ktiopo 4. *Applied physics letters*, 74(7):914–916, 1999.

[13] Christopher Gerry, Peter Knight, and Peter L Knight. *Introductory quantum optics*. Cambridge university press, 2005.

[14] GN Gol'Tsman, O Okunev, G Chulkova, A Lipatov, A Semenov, K Smirnov, B Voronov, A Dzardanov, C Williams, and Roman Sobolewski. Picosecond superconducting single-photon optical detector. *Applied physics letters*, 79(6):705–707, 2001.

[15] Antony Winata Haranto. Characterization of single-photon detectors with tightly time-correlated photon pairs. UROPS report, National University of Singapore, 2020.

[16] C. K. Hong, Z. Y. Ou, and L. Mandel. Measurement of subpicosecond time intervals between two photons by interference. *Phys. Rev. Lett.*, 59:2044–2046, Nov 1987.

[17] Feiyan Hou, Runai Quan, Ruifang Dong, Xiao Xiang, Baihong Li, Tao Liu, Xiaoyan Yang, Hao Li, Lixing You, Zhen Wang, et al. Fiber-optic two-way quantum time transfer with frequency-entangled pulses. *Physical Review A*, 100(2):023849, 2019.

[18] AM Kadin and MW Johnson. Nonequilibrium photon-induced hotspot: A new mechanism for photodetection in ultrathin metallic films. *Applied Physics Letters*, 69(25):3938–3940, 1996.

[19] Hamamatsu Photonics K.K. Hamamatsu r5509-73 datasheet. `https:`

//www.hamamatsu.com/jp/en/product/optical-sensors/pmt/pmt_tube-alone/head-on-type/R5509-73.html, last accessed on 30-03-2022.

[20] Hamamatsu Photonics K.K. *Photomultiplier tubes basics and applications fourth edition.* Hamamatsu Photonics K.K., 2017.

[21] Andrew M. Kowalevicz and Frank Bucholtz. Beam divergence from an smf-28 optical fiber. 2006.

[22] Aaron J. Miller, Adriana E. Lita, Brice Calkins, Igor Vayshenker, Steven M. Gruber, and Sae Woo Nam. Compact cryogenic self-aligning fiber-to-detector coupling with losses below one percent. *Optical express*, 19(10):9102–9110, May 2011.

[23] Anna Mukhtarova, Luca Redaelli, Dibyendu Hazra, Houssaine Machhadani, Stéphane Lequien, Max Hofheinz, Jean-Luc Thomassin, Frederic Gustavo, Julien Zichi, Val Zwiller, et al. Polarization-insensitive fiber-coupled superconducting-nanowire single photon detector using a high-index dielectric capping layer. *Optics Express*, 26(13):17697–17704, 2018.

[24] Chandra M Natarajan, Michael G Tanner, and Robert H Hadfield. Superconducting nanowire single-photon detectors: physics and applications. *Superconductor science and technology*, 25(6):063001, 2012.

[25] Gadman Optics. Ktp crystal physical properties. https://www.gamdan.com/ktp, last accessed on 21-03-2022.

[26] OZ optics. Tapered fiber specifications. https://shop.ozoptics.com/tsmj-x-1550-9125-025-7-2-12-2-ar, last accessed on 30-03-2022.

[27] PicoQuant. Time-correlated single photon counting. https://www.picoquant.com/images/uploads/page/files/7253/technote_tcspc.pdf, last accessed on 2-04-2022.

[28] Charles P Poole, Horacio A Farach, and Richard J Creswick. *Superconductivity.* Academic press, 2013.

[29] Alex D Semenov, Gregory N Gol'tsman, and Alexander A Korneev. Quantum detection by current carrying superconducting film. *Physica C: Superconductivity*, 351(4):349–356,

2001.

[30] Lijiong Shen, Jianwei Lee, Antony Winata Hartanto, Pengkian Tan, and Christian Kurtsiefer. Wide-range wavelength-tunable photon-pair source for characterizing single-photon detectors. *Optics Express*, 29(3):3415–3424, 2021.

[31] Poh Hou Shun. Towards a high quality polarization-entangled multi-photon source. Master's thesis, National University of Singapore, 2009.

[32] Thorlabs. Grin lens specifications. `https://www.thorlabs.com/newgrouppage9.cfm?objectgroup_id=1209`, last accessed on 30-03-2022.

[33] Thorlabs. Smf-28 specifications. `https://www.thorlabs.com/drawings/45c5717eb643c372-BCB58E62-FC52-C191-4E53080FBCF43FE0/SMF-28-J9-SpecSheet.pdf`, last accessed on 26-03-2022.

[34] Michael Tinkham. *Introduction to superconductivity.* Courier Corporation, 2004.

[35] Guang-Zhao Xu, Wei-Jun Zhang, Li-Xing You, Jia-Min Xiong, Xing-Qu Sun, Hao Huang, Xin Ou, Yi-Ming Pan, Chao-Lin Lv, Hao Li, et al. Superconducting microstrip single-photon detector with system detection efficiency over 90% at 1550 nm. *Photonics Research*, 9(6):958–967, 2021.

[36] Lixing You. Superconducting nanowire single-photon detectors for quantum information. *Nanophotonics*, 9(9):2673–2692, 2020.

[37] AN Zotova and D Yu Vodolazov. Photon detection by current-carrying superconducting film: A time-dependent ginzburg-landau approach. *Physical Review B*, 85(2):024509, 2012.